CHARACTERIZATION OF NUCLEAR REACTOR PRESSURE VESSEL (RPV) SURROGATE SPECIMENS WITH ULTRASOUND

A Thesis
Presented to
The Academic Faculty

by

Katherine Scott

In Partial Fulfillment
of the Requirements for the Degree
Master of Science in the
G.W. Woodruff School of Mechanical Engineering

Georgia Institute of Technology
December 2016

CHARACTERIZATION OF NUCLEAR REACTOR PRESSURE VESSEL (RPV) SURROGATE SPECIMENS WITH ULTRASOUND

Approved by:

Dr. Laurence Jacobs, Advisor
School of Mechanical Engineering
Georgia Institute of Technology

Dr. Jin-Yeon Kim
School of Civil Engineering
Georgia Institute of Technology

Dr. Karim Sabra
School of Mechanical Engineering
Georgia Institute of Technology

Date Approved: December 06, 2016

ACKNOWLEDGEMENTS

I would first like to thank my wonderful advisors, Dr. Laurence Jacobs and Dr. Jin-Yeon Kim. Without their help and guidance, I would not have learned nearly as much. Through their support, I was able to learn about this area of nonlinear linear ultrasound, a field that I was unfamiliar with coming into graduate school. They not only taught me how to make and understand the measurements but also how to be a researcher. I would like to thank them for giving me this opportunity to complete my masters and conduct research in this field. I would also like to thank Dr. Karim Sabra for agree to be on my thesis committee as well as being a great teacher in the areas of wave propagation and acoustics.

I would like to thank Dr. Duck-Gun Park for providing us with the specimens for this research. Dr. Park also was a great help by providing the microscopy of the specimens. I would have been unable to conduct this research without the use of the furnace provided by Dr. Preet Singh which I am very grateful.

I would also like to thank the NEUP for my wonderful fellowship, the Integrated University Program Graduate Fellowship. This material is based upon work supported under an Integrated University Program Graduate Fellowship.

I would like to thank the two undergraduates who worked with me on this research. I would like to thank Kayla Andrews for her help polishing the Fe-1.0% Cu specimens. I would like to thank Devin Roach for his help heat treating and polishing the Fe-0.1% Cu specimens.

Further, I would like to thank all of my lab mates for all of their support and help, David Torello for teaching me how to make measurements, all of the subsequent help after

that, and for being a good friend, Gun Kim for teaching me about grad school, helping me with my measurements, teaching about SHG, and for being a good friend, and to everyone else who provided support: Alex Lakocy, Matt Uhrig, Toby Oberhardt, Aulon Bajrami, Marc Forstenhaeusler, Daniel Grun, Chris Doerr, and Mehdi Rashidi. Additionally, I would like to thank Katie Cook for her vast insight into nuclear reactors and her help for anything nuclear related.

Finally, I would like to thank Bryan Levy. Without his help and support, this would not have been possible. From late night measurement sessions to helping me practice presentations, I would never have been able to come so far.

TABLE OF CONTENTS

LIST OF TABLES

LIST OF FIGURES

LIST OF SYMBOLS AND ABBREVIATIONS

RPV	reactor pressure vessel
Fe	iron
Cu	copper
NLU	nonlinear ultrasound
NDE	nondestructive evaluation
SHG	second harmonic generation
β	nonlinearity parameter
ω	angular frequency
ρ	material density
u	particle displacement
σ	stress
E_1	second order elastic constant
E_2	third order elastic constant
C_{11}	second order Brugger elastic constant
C_{111}	third order Brugger elastic constant
c_l	longitudinal wave speed
A_1	amplitude of fundamental frequency
A_2	amplitude of second harmonic
k	wave number
τ	shear stress
R	Schmid factor
T	line tension

G	shear modulus
b	Burgers vector
Λ	dislocation density
Ω	conversion factor from shear strain to longitudinal strain
γ	shear strain
ε	longitudinal strain
δ	lattice misfit parameter
L	half of dislocation segment length
r_1, r_c	precipitate radius, critical radius
f_n, f_g	volume fraction critical nuclei and growing nuclei
h_i	distance above specimen
D	diffraction correction
a	diameter of transducer
V_i	amplitude of reflection
α	attenuation
t_f	time
Mn	manganese
Ni	nickel
Si	silicon
DBTT	ductile-to-brittle transition temperature
CVN	Charpy-V-notch
BCC	body-centered cubic
FCC	face-centered cubic
KAERI	Korean Atomic Energy Research Institute
SANS	small-angle neutron scattering

FFT	fast Fourier transform
A_k	amplitude Prony method
f	frequency
B	bulk modulus
v_i	volume
β_L	lattice nonlinearity parameter

SUMMARY

This research determines the sensitivity of nonlinear ultrasound (NLU) to the changes in microstructure of heat treated Fe-1.0% Cu and Fe-0.1% Cu binary alloys. The Fe-Cu material investigated in this research serves as a surrogate material to simulate the evolution of radiation damage that occurs in reactor pressure vessels (RPVs) of light water reactors (LWRs). The formation of the Cu-precipitates in RPV steel is one of the main factors leading to radiation embrittlement. With RPVs seeing more neutron irradiation than originally anticipated, developing nondestructive evaluation (NDE) techniques capable of evaluating the integrity of these structures is highly desirable. This research investigates the sensitivity of the NLU technique, second harmonic generation (SHG), to the changes in the surrogate material microstructure. It is experimentally observed that as the surrogate material is heat treated the nucleated Cu-precipitates grow up to a few nanometers and then coarsens.

For the experimental procedure used in this research, ultrasonic longitudinal waves are propagated through the thickness of the specimens where higher harmonics are generated. The nonlinearity parameter, β, can then be calculated by relating the amplitude of the fundamental frequency to the amplitude of the second harmonic wave. Additionally, a theoretical model was applied to relate the change in β to the change in the Cu-precipitate radius. As will be seen in the results, there is a signification increase in β for the Fe-1.0% Cu specimens in contrast to there being little change in β for the Fe-0.1% Cu specimens. The significant increase in β demonstrates the sensitivity of SHG to these Cu-precipitates.

CHAPTER 1. INTRODUCTION

1.1 Motivation and Objectives

With the nuclear industry in the United States entering the first period of life extension, light water power reactors will see more neutron exposure and duty cycles than were originally anticipated. While remaining life may be determined using destructive tests, this is not always a viable option. Therefore, it is very important to develop nondestructive evaluation (NDE) techniques to access damage due to chronic radiation exposure in these nuclear reactor pressure vessel (RPV) steels. These techniques will be one of the keys that will help provide the nuclear industry with a technical basis for a second life extension (operation to 80 years).

When looking at ultrasonic NDE techniques, the decision must be made between the use of conventional linear ultrasonic techniques or nonlinear ultrasonic (NLU) techniques. Linear ultrasound is known to be able to detect damage that is on the same order of magnitude as the wavelength of the ultrasonic wave where as NLU is known to be able to detect microstructural damage that is orders of magnitudes smaller than the wavelength of the ultrasonic wave. For the material investigated in this research, it will be shown that the microstructural damage (Cu-precipitates) is on the order of nanometers, while the wavelength is on the order of millimeters. With the damage being so small in this material, it is desirable to use NLU as this will allow for the use of ultrasonic waves in the 2-5 MHz range which is a realistic capability of the experimental setup.

To date, work has been done demonstrating the sensitivity of NLU techniques to irradiation damage [1-4]. However, irradiation embrittlement is caused by a variety of different mechanisms as will be describe in CHAPTER 3. Therefore, it is important to separate these variables in order to determine the contribution of each to the sensitivity of NLU. This is accomplished through the use of surrogate specimens. Not only do surrogate specimens control the type of damage that will occur in these specimens, but also provides a specimen that can easily and safely be handled in a laboratory setting instead of a hot cell.

This research focuses on a very important embrittlement variable which is the precipitation of Cu that occurs during irradiation. In order to do this, two sets of Fe-Cu surrogate specimens, 0.1% and 1.0% by weight of Cu, were investigated. Fe-Cu binary alloys is a material that is well known to simulate radiation damage [5-8]. As Fe-Cu is heat treated, the Cu-precipitates in the material grow in size simulating different amounts of radiation damage.

The sensitivity of NLU to the growth of these Cu-precipitates was investigated through the use of the NLU technique, second harmonic generation (SHG). SHG is a technique where a single frequency wave propagating in a nonlinear elastic material will generate higher harmonics as it interacts nonlinearly with the microstructure of the material [9]. The amplitude of the fundamental frequency is then related to that of the second harmonic resulting in the acoustic nonlinearity parameter, β. β values for each of the heat treated surrogate specimens can be compared to determine the sensitivity of SHG to these Cu-precipitates.

1.2 Previous Work: SHG

SHG has been shown in many publications to be sensitive to microstructural damage in a variety of materials. The benefit of using SHG is the ability to detect microstructural damage that is orders of magnitudes smaller than the wavelength of the introduced ultrasonic wave in contrast to linear ultrasonic methods that can only detect damage that is on the same scale as the wavelength of the wave. It has been shown that microstructural features such as dislocations [10], dislocation dipoles [11], and precipitates [12] can be detected with SHG. Hurley et al studied the precipitation of Cu-rich precipitates in ASTM A710 steel where the nonlinearity parameter was compared to inhomogeneous strain [13]. Viswanath et al studied the change in the relative nonlinearity parameter of M250 maraging steel as it was heat treated for varying lengths of time [14]. Another study developed a procedure to relate the nonlinearity parameter to the fracture toughness of the material [15]. All of these studies show the ability of SHG to detect microstructural changes in the material.

1.3 Structure of Thesis

This thesis will start off in Chapter 2 by deriving the equations needed to calculate the acoustic nonlinearity parameter. Extensions of these relationships will then be made to theoretically calculate the acoustic nonlinearity parameter for the specific microstructural condition of precipitate pinned dislocations. It will be assumed that the nonlinearity in the Fe-Cu specimens is due to the Cu-precipitates pinning dislocations. Finally, the end of Chapter 2 will give a brief description of how the attenuation and velocity in the specimens was calculated.

Moving on from the theoretical background of NLU, Chapter 3 will give a brief background on radiation embrittlement. This chapter will set up the context for the need of the surrogate specimens studied in this research as well as provide a description of the current evaluation method of RPV steels.

Chapter 4 will provide a more in depth look at the surrogate material. It will provide the background for the evolution of the Cu-precipitates. It will also discuss the radii of the Cu-precipitates as well as the hardness that was measured for these specific specimens.

Looking to Chapter 5, an in-depth description of the experimental procedure will be discussed. This chapter first looks at the preparation of the specimens and then delves into the actual experimental method used to make the NLU measurements.

The next chapter, Chapter 6, discusses the results from both the NLU and linear ultrasound measurements. The nonlinear results for both sets of surrogate specimens will be investigated and compared. Additionally, an existing theoretical model will be used for the change in the nonlinearity parameter and will be compared to the experimental results for the Fe-1.0% Cu specimens.

Chapter 7 provides conclusions of the thesis as well as some ideas for future work that may be done in this field of study.

CHAPTER 2. NONLINEAR ELASTIC WAVE PROPAGATION

2.1 Derivation of the Nonlinearity Parameter

Consider a single frequency sinusoidal longitudinal wave whose angular frequency is ω. This wave propagates in the x-direction through the thickness of a nonlinear, isotropic, elastic material where the equation of motion [10, 16] in one direction can be written as Equation (1)

$$\rho \frac{\partial^2 u}{\partial t^2} = \frac{\partial \sigma_{xx}}{\partial x} \tag{1}$$

where ρ is the density of the material, u is the particle displacement, and σ_{xx} is the normal stress in the x-direction. This material has a quadratic nonlinear relationship between stress and strain so the normal stress [10] can be written as Equation (2)

$$\sigma_{xx} = \sigma_0 + E_1 \frac{\partial u}{\partial x} + \frac{1}{2} E_2 \left(\frac{\partial u}{\partial x}\right)^2 \tag{2}$$

where σ_0 is the pre-existing stress in the material, E_1 is the second order elastic constant and E_2 is the third order elastic constant. It is also known that the material nonlinearity parameter, β, for a material in its virgin state has a relationship with the second and third order elastic constants as can be seen in Equation (3). Equation (3) written in terms of the second and third order Brugger elastic constants is given as:

$$\beta = -\frac{E_2}{E_1} = -\left(\frac{3C_{11} + C_{111}}{\sigma_0 + C_{11}}\right) \tag{3}$$

Combining the constitutive equation for quadratic nonlinearity, the equation of motion, and the relationship for β, one can derive the nonlinear wave equation[10] Equation (4) in one-direction to be

$$\frac{\partial^2 u}{\partial t^2} = {c_l}^2 \left[1 - \beta \frac{\partial u}{\partial x}\right] \frac{\partial^2 u}{\partial x^2} \tag{4}$$

where c_l is the longitudinal wave speed in the material. A perturbation solution to this wave equation which will be considered in this paper can be written in Equation (5) [10].

$$u_{out} = A_1 \sin(kx - \omega t) + \frac{\beta {A_1}^2 x k^2}{8} \sin(2kx - 2\omega t) + \cdots \tag{5}$$

This solution takes into consideration that as a propagating wave travels through the material and interacts with the microstructure, higher harmonic waves will be generated (ie. 2ω, 3ω, etc.) [10, 17] where the amplitude of the second harmonic seen in the second part of Equation (5) is found to be equal to

$$A_2 = \frac{\beta {A_1}^2 x k^2}{8} \tag{6}$$

By rearranging Equation (6) with respect to β, an equation (7) for the material nonlinearity parameter can be found, and it can be seen that acoustic nonlinearity parameter is proportional to the ratio of A_2 to ${A_1}^2$:

$$\beta = \frac{8A_2}{x k^2 {A_1}^2} \propto \frac{A_2}{{A_1}^2} \tag{7}$$

With this knowledge, the value for a relative β can easily be determined through the measurement of the amplitudes of the first and second harmonic waves. It is important to

note that this calculation of β assumes plane wave propagation as well as the absence of attenuation, diffraction, and scattering.

2.2 Contribution of Microstructural Damage to Nonlinearity

In the Fe-Cu specimens investigated in this research, it is known that Cu-precipitates nucleate and grow as the thermal aging of the material progresses (for more information see CHAPTER 4). As these precipitates grow, they interact with the dislocations in the base Fe matrix. These precipitates act as pinning points causing a bending of the dislocation segment. Figure 1 shows a three-point bending scenario of the interaction of the dislocation segment with the precipitates.

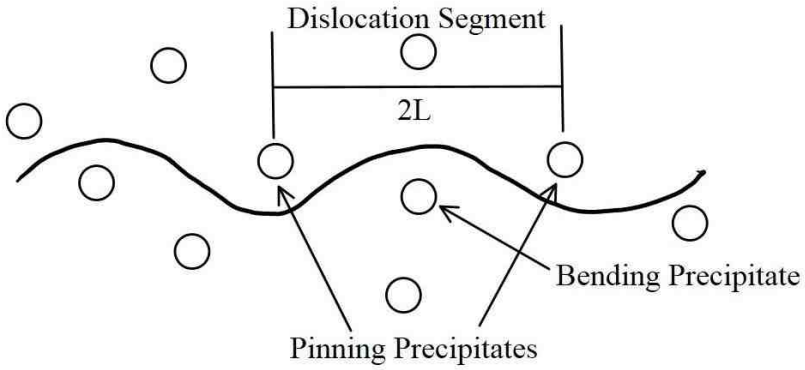

Figure 1. Pinned Dislocation Segment

2.2.1 Dislocation contribution to nonlinearity parameter

Before one can understand the effect of precipitate pinned dislocations on the nonlinearity parameter of the material, the effect of just pinned dislocations should be determined. Hikata et al. developed a model for the effect of pinned dislocations in a material on the acoustic nonlinearity parameter [10]. In their model, they considered a

pinned edge dislocation which is lying in the slip plane of an isotropic crystal. If a longitudinal stress, σ, is applied to this dislocation segment, the dislocation segment will bow and form a circular arc of radius, r. In this model, it is assumed that the dislocation density is low enough that the interaction between dislocations can be ignored. This longitudinal stress can be related to the shear stress through the use of the Schmid factor, R: $\tau = R\sigma$. Equation (8) shows the relationship between this shear stress and the line tension, T, due to the applied stress where G is the shear modulus and b is the Burgers vector.

$$\tau = \frac{T}{rb} = \frac{Gb}{2r} \tag{8}$$

In relationship to the shear stress, the corresponding shear strain can be determined using Equation (9) where Λ is the dislocation density, L is half the dislocation segment length, and S is the area swept by the dislocation segment ($S = r^2\left(\theta - \frac{1}{2}\sin(2\theta)\right)$. Plugging in for the area swept by the dislocation segment and assuming that θ is small, one can solve for the second answer of Equation (9).

$$\gamma_d = \frac{\Lambda b}{2L}S = \frac{2\Lambda L^2}{3G}r + \frac{4\Lambda L^4}{5G^3b^2}r^3 \tag{9}$$

Knowing this information about the shear strain from the dislocation segment motion, the total longitudinal strain can be determined by adding the dislocation strain and the lattice strain as can be seen in Equation (10) where Ω is the conversion factor from shear strain to longitudinal strain.

$$\varepsilon = \varepsilon_l + \Omega\gamma_d \tag{10}$$

Using the longitudinal stress-longitudinal strain relationship seen in Equation (2) to determine the strain from the lattice, the total strain in the material can solved for as seen in Equation (11).

$$\varepsilon = \left(\frac{1}{E_1} + \frac{2\Omega\Lambda L^2 R}{3G}\right)\sigma + \frac{E_2}{{E_1}^3}\sigma^2 + \frac{4\Omega\Lambda L^4 R^3}{G^3 b^2}\sigma^3 \tag{11}$$

Now consider that an additional oscillatory stress, $\Delta\sigma$, is applied to the dislocation segment in addition to σ. This additional stress will cause the dislocation segment to move even further causing an additional strain, $\Delta\varepsilon$. $\Delta\sigma$ is a function of $\Delta\varepsilon$ and can be written as seen in Equation (12).

$$\begin{aligned}\Delta\sigma = &\left[\frac{1}{E_1} + \frac{2\Omega\Lambda L^2 R}{3G}\right]^{-1}\Delta\varepsilon \\ &- \left[\frac{E_2}{{E_1}^3} + \frac{12\Omega\Lambda L^4 R^3}{5G^3 b^2}\sigma\right]\left[\frac{1}{E_1} + \frac{2\Omega\Lambda L^2 R}{3G}\right]^{-3}\Delta\varepsilon^2\end{aligned} \tag{12}$$

By comparing the form of Equation (12) to that of Equation (2), it can be seen that the nonlinearity parameter is the negative ratio of the coefficients in the stress equation. Using this knowledge an expression of the total nonlinearity of the material can be written as

$$\beta_{tot} = \left[-\frac{E_2}{{E_1}^3} + \frac{24\Omega\Lambda L^4 R^3}{5G^3 b^2}\sigma\right]\left[\frac{1}{E_1} + \frac{2\Omega\Lambda L^2 R}{3G}\right]^{-3} \tag{13}$$

For most materials, it can be assumed that $\frac{2\Omega\Lambda L^2 R}{3G}$ is much, much smaller than $\frac{1}{E_1}$. Therefore, β_{tot} can be written as

$$\beta_{tot} = \left[-\frac{E_2}{E_1} + \frac{24\Omega\Lambda L^4 R^3 {E_1}^2}{5G^3 b^2}\sigma \right] \tag{14}$$

As was seen in Equation (3), the lattice contribution to the nonlinearity parameter is $\beta_0 = -{E_2}/{E_1}$. From this relationship of the lattice contribution, the change in the nonlinearity parameter due to pinned dislocations can be determined and is seen in Equation (15). Note that in order to evaluate this equation, one needs to know the stress applied on the dislocation segment.

$$\Delta\beta = \frac{24}{5}\frac{\Omega\Lambda L^4 R^3 {E_1}^2 |\sigma|}{G^3 b^2} \tag{15}$$

2.2.2 Precipitate pinned dislocation contribution to the nonlinearity parameter

Cantrell and Yost later used the relationship in Equation (15) to quantify the change in the nonlinearity parameter by plugging the stress caused by a precipitate into Equation (15) and applied the derived formula to evaluate the precipitation process in an aluminum alloy [18]. This model assumes that the precipitates are randomly distributed throughout the material. It also assumes that the precipitates are spherical in shape and are elastically isotropic, and the stress is due to misfit between the lattice structures of the precipitate and the matrix. The main addition to the Hikata et al. model is the definition of the radial stress.

Here the radial stress is assumed to be caused by the spherical precipitates randomly embedded in the matrix of the material. Equation (16) shows this relationship between the stress and the radius of the precipitate where δ is the misfit parameter between the precipitate and the matrix and r_1 is the radius of the spherical precipitate.

$$\sigma = -\frac{4G\delta {r_1}^3}{\left({L}/{2}\right)^3} \tag{16}$$

Plugging this expression for the radial stress (Equation (16)) into Equation (15) one will get Equation (17) for the change in the nonlinearity parameter due to a dislocation segment that is pinned by precipitates.

$$\frac{\Delta\beta}{\beta_0} = 154\frac{\Omega\Lambda L R^3 {C_{11}}^2 |\delta| {r_1}^3}{\beta_0 G^2 b^2} \tag{17}$$

As can be seen in Equation (17), all of the variables except for L and r_1 are material constants and are therefore not dependent on the growth of the precipitate. However, since L and r_1 are dependent on the nucleation and growth of the precipitates, it is important to develop relationships to calculate each of these quantities. The radius of the precipitate is known to be a function of the critical radius, r_c, the volume fraction of critical nuclei, f_n, and the volume fraction of growing nuclei, f_g as can be seen in Equation (18). The critical radius is defined to be the statistical radius at which the nucleation of a precipitate occurs.

$$r_1 = r_c\left(1 + \frac{f_g}{f_n}\right)^{1/3} \tag{18}$$

Since the precipitates are randomly distributed throughout the matrix, the distance, L, between the precipitates is dependent on the volume fraction of critical nuclei as well as the critical radius as can be seen in Equation (19).

$$L = \left(\frac{4\pi}{3}\right)^{1/3}\frac{r_c}{{f_n}^{1/3}} \tag{19}$$

Now that the equations for the radius of the precipitate and the distance between precipitates are known, they can be substituted back into Equations (17) to finally obtain the relationship between precipitate pinned dislocations and the nonlinearity parameter as seen in Equation (20). If one were to know the material properties of the specimens that they were investigating, one would be able to develop a theoretical model for the change in the nonlinearity parameter as a function of precipitate growth.

$$\frac{\Delta\beta}{\beta_0} = 248\frac{\Omega\Lambda R^3 {C_{11}}^2 |\delta| {r_{crit}}^4}{\beta_0 G^2 b^2}\left({f_n}^{-1/3} + {f_n}^{-4/3} f_g\right) \tag{20}$$

CHAPTER 3. RADIATION EMBRITTLEMENT IN RPV STEEL

3.1 Radiation Embrittlement Mechanisms

The chronic radiation exposure that is seen by these light water power reactors leads to the embrittlement of the RPV steels [19, 20]. While embrittlement in the RPV steels is a very complicated process and depends on many variables such as chemical composition, neutron fluence, neutron flux, irradiation temperature, etc., studies have shown that this embrittlement is caused by a combination of multiple microstructural changes [21]. Examples of these microstructural changes include vacancies, microvoids, dislocation loops, and the formation of precipitates including clusters enriched with Cu, Mn, Ni, and Si, as well as phosphide formations, and carbide formations [19-23].

Despite the complexity of embrittlement, the causes of irradiation embrittlement on a basic level can be broken down into two main material changes [24, 25]. One material change, radiation hardening, is considered to be the major contributor to embrittlement. Radiation hardening will be described in more detail later on in this chapter. The second material change is the segregation of precipitates along the grain boundaries. This segregation of precipitates along grain boundaries can result in intergranular failure. Precipitates that typically move to grain boundaries causing this intergranular failure include phosphorus and sulfur.

3.1.1 Radiation Hardening

Radiation embrittlement is typically characterized by an increase of the ductile-to-brittle transition temperature (DBTT). The DBTT indicates the transition temperature

between the low toughness brittle fracture region and the high toughness ductile fracture region. In this section, the focus on the mechanism causing this increase in DBTT will be material hardening. As precipitates nucleate and grow in RPV steel, the precipitates provide an obstacle to the motion of dislocations in the material. This hindrance to motion results in a hardening of the material, as described in more detail in Section 4.4. This hindrance of motion also leads to an increase in the yield strength of the material [20, 25-27]. This increase in the yield strength of the material induces an increase in the DBTT.

While there are many precipitates that form in RPV steel as irradiation occurs such as Mn, Ni, and Si, Odette et al have provided considerable evidence the main contribution to this hardening and consequently embrittlement is Cu rich precipitates (CRPs) [26, 27]. In many of the RPVs in the United States, there is a significant amount of Cu present in the RPV steel coming from the use of recycled steel [21, 25]. Since Cu is one of the main variables contributing to radiation embrittlement and significant amounts of Cu can be found in RPV steel, it is desired to study these Cu-precipitates through the use of surrogate specimens.

3.2 Current Surveillance and Monitoring Methods

Currently, the only method of surveillance for RPVs is through destructive tests. The standard method is the placement of samples made out of the same RPV steel, typically Charpy-V-notch impact specimens (CVN), inside the RPV at the startup of the RPV. These samples are placed in areas of the RPV where the neutron flux is much higher than the RPV will experience itself. This placement allows for the integrity of the RPV to be monitored, and these samples provide a projective model for the RPV itself. Periodically

during reactor shutdowns, a CVN is removed from the RPV and a Charpy impact test is performed allowing for the determination of the DBTT [20, 26-28]. A practical issue with the CVN specimen based DBTT determination is that the CVN specimens initially placed at the start of the RPVs are running out as the design life of the RPVs are ending. Additional sets of CVN specimens could be placed but how to relate the DBTT based on new CVN specimens to the actual DBTT of RVP steels remains an open question to be answered.

CHAPTER 4. FE-CU SURROGATE SPECIMENS

4.1 Overview

The use of surrogate specimens to simulate different types of damage provides many benefits in this field of research. Instead of having to travel to a specific site to make in situ measurements and use any protective measures required for that environment, surrogate specimens allow for measurements to easily be made in a laboratory environment. In addition, surrogate specimens provide a method to separate variables that might be affecting the microstructure of the material. This separation of variables allows for the study of each effect separately and reduces any compounding effects that might be occurring in the measurements being made. A better understanding of each individual variable allows for a better understanding of the initial material as a whole. This understanding allows for better and more accurate results in situ.

This research focuses on one of the critical variables which contributes to the embrittlement that occurs during radiation, the formation of Cu-precipitates as discussed in Section 3.1.1. Therefore, it is very important to study the effect that these precipitates have on the sensitivity of SHG. This formation of Cu-precipitates can be simulated through the use of Fe-Cu surrogate specimens.

Two sets of surrogate specimens (six specimens per set) were manufactured through the melting of pure Fe and pure Cu at the Korean Atomic Energy Research Institute (KAERI). One set contained 1.0% by wt. Cu, and the second set contained 0.1% by wt. Cu. Both sets of specimens were thermally aged for varying amounts of time at 500°C. Since

there were six specimens in each set of surrogate specimens, one specimen from each set was set aside as a baseline specimen and the remaining five specimens from each set were heat treated using the following heat treatment schedule: 5 hours, 15 hours, 30 hours, 100 hours, and 300 hours, respectively. This thermal aging promotes the nucleation and growth of Cu-precipitates and simulates different amounts of radiation damage. More details of the manufacturing and heat treatment of these specimens can be seen in Section 5.1.

4.2 Interaction between Cu-precipitate and matrix

The Fe-Cu specimens investigated in this research are a very similar to Fe-Cu material that has been studied extensively in the past. Many experimental measurements as well as computer simulations have been performed in order to better understand the evolution of these Cu-precipitates and their interaction with the α-iron matrix as heat treatment time increases. In particular, the coherency of the Cu-precipitates and the α-iron matrix as precipitate radius grows is of interest.

It is well known that as the Fe-Cu material is heat treated the structure of the Cu-precipitates transforms from the coherent BCC (body-centered cubic) structure to semi-coherent 9R structure to incoherent FCC (face-centered cubic) structure[29-34]. Many studies have been performed to determine the critical transition radius for each of these structural transitions. Othen et al. showed that this transformation from BCC to 9R occurs when the Cu-particle size is between 4 to 5 nm and the transformation from 9R to FCC occurs when the Cu-particle size is approximately 18 nm [33].

4.3 Precipitate Radii of Fe-1.0% Cu Specimens

Microscopy measurements were performed on an identical set of Fe-1.0% Cu specimens at KAERI. These microscopy measurements included the determination of the Cu-precipitate radii as a function of heat treatment time through small-angle neutron scattering (SANS) measurements conducted at the HANARO reactor [35]. These SANS measurements were completed using a neutron wavelength of 4.31 Å and a magnetic field of 1.2 tesla. Figure 2 displays a graphical representation of these measurements and Table 1 displays the actual values of the exact radii measured. As can be seen from the figure, the radii of the Cu-precipitates increased as a function of increasing heat treatment time which was expected. While SANS data was only collected for heat treatment times of 5 hours to 100 hours, it is presumed that the precipitate radii will continue to increase as the heat treatment time is increased to 300 hours.

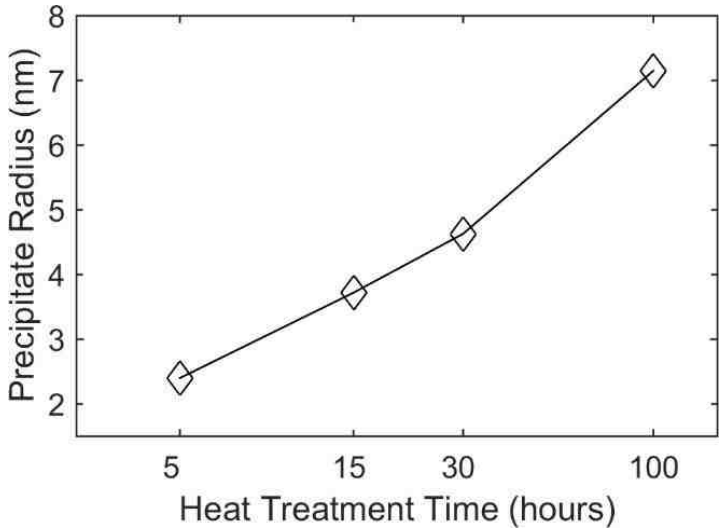

Figure 2. Cu-precipitate radius for Fe-1.0% Cu specimens

Table 1. Cu-precipitate radius of Fe-1.0% Cu specimens

Heat Treatment Time (hours)	5	15	30	100
Radius (nm)	2.4	3.72	4.63	7.15

As can be seen from Figure 2 and Table 1, at a heat treatment time of 30 hours, the radius of the Cu-precipitates is 4.63 nm. This indicates that a transition of the Cu-precipitates from BCC structure to 9R structure might be occurring after the 30 hour specimen. This conclusion is drawn from the fact that this radius falls in the transition range that was discussed in Section 4.2. While the precipitate radius continues to increase as heat treatment time increases, it is presumed that this set of specimens never reaches the transition from the 9R structure to the FCC structure because the largest precipitate radii observed is 7.15 nm (while there is no data for the 300-hour specimen the precipitate radii is expected to be slightly larger than 7.15 nm) which is way below the transition radius of 18 nm as discussed in Section 4.2

4.4 Vickers Hardness Measurements Fe-1.0% Cu

Many studies have shown that as the radius of the Cu-precipitates grows there is hardening of the material and after a critical radius there is a transition to softening of the material [31, 34, 36, 37]. The initial hardening of the material is due to the Cu-precipitates creating a stress that provides a resistance to the dislocation motion. This initial hardening occurs when the precipitates have a BCC structure such that the precipitates have a coherent lattice structure with the matrix's. However, as the precipitates transition from the BCC structure to the 9R structure, there is an increase in the distance between Cu-clusters which

changes the stress that is present on the matrix which consequently no longer induces as large of a resistance to the dislocation motion. This leads to the softening of the material.

Vickers hardness measurements were also made by Park et al on an identical set of Fe-1.0% Cu specimens [38]. Figure 3 displays these Vickers hardness measurements. As can be seen, there is an initial increase in the hardness of the material followed by softening of the material as was to be expected. This softening begins after the 30-hour specimen. This is what was expected because it was predicted that the transition from the BCC structure to the 9R structure occurred for this specimen as was discussed in Section 4.4.

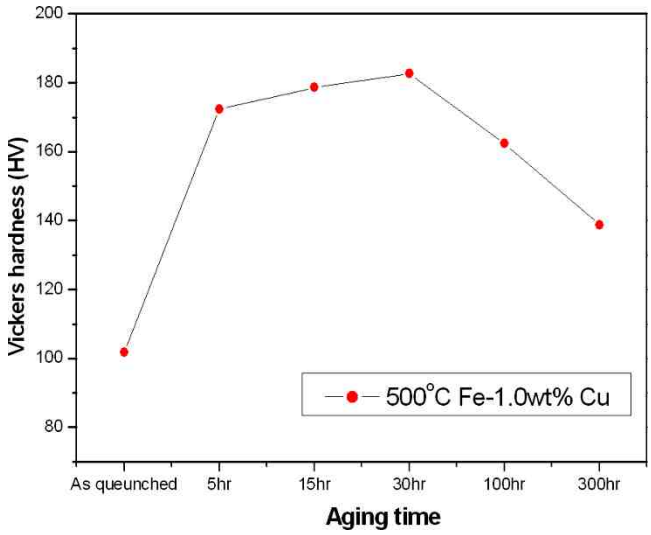

Figure 3. Vickers hardness measurements [38]

CHAPTER 5. EXPERIMENTAL PROCEDURE

5.1 Surrogate Specimen Preparation

The Fe-1.0% Cu and Fe-0.1% Cu surrogate specimens used in this research were manufactured at the Korean Atomic Energy Research Institute (KAERI). The material was manufactured by melting pure Fe and pure Cu. The material was then solution treated in a vacuum at a temperature of 850°C for five hours. Finally, the material was water-quenched to make two sets of binary alloy specimens, Fe-0.1% Cu and Fe-1.0% Cu [38]. Once manufactured, these specimens were sent to the researcher's lab for further specimen preparation.

5.1.1 Heat Treatment

Both the Fe-1.0% Cu and Fe-0.1% Cu specimens underwent a heat treatment schedule. This heat treatment schedule caused the nucleation and growth of Cu-precipitates in this material simulating one feature of radiation damage that occurs in RPV steels as was explained in CHAPTER 3. Each set of Fe-Cu material consisted of 6 specimens all manufactured using the same process, as described at the beginning of the section, resulting in a total of 12 specimens, six Fe-0.1% Cu and six Fe-1.0% Cu. From each set of specimens, one specimen was set aside as the baseline, untreated specimen. Each of the remaining specimens was heat treated following the following schedule respectively, 5 hours, 15 hours, 30 hours, 100 hours, and 300 hours. The heat treatment was performed in a furnace at a temperature of 500°C. Throughout the heat treatment cycle, the temperature of the furnace was monitored regularly through the use of a thermocouple in order to ensure that

the temperature of the furnace remained 500°C. After the completion of the heat treatment time, the specimen was carefully removed from the oven and placed on a concrete block. After the specimen was taken out of the furnace, the specimen remained untouched and was allowed to gradually cool at room temperature.

5.1.2 Surface Treatment

When making NLU measurements, it is very important to have smooth (almost mirror like) surface conditions. Since the through thickness measurements require the use of both sides of the material, smooth surface conditions are desired on both sides of the specimen. In order to achieve these conditions after heat treatment, these specimens were taken to ME machine shop at Georgia Tech for initial surface conditioning. Initially, a low stress machining and a surface grind was performed on each of the specimens. Both of these steps were done to remove the fire scale that formed on the surface of the materials during heat treatment. Next, each specimen was sanded using sand paper from 80 grit to 2000 grit. The sanding was done on each side of the specimen, and the grit was only increased after the effects of the previous grit were no longer visible. Figure 4 displays a sample surrogate specimen before and after surface preparation. After preparation, it was found that the dimensions of the specimens are 150 mm x 32 mm x 9.4 mm thick.

Figure 4. Top:Specimen after heat treatment, Bottom:Specimen after surface preparation

5.2 Nonlinear Ultrasonic Measurement Setup and Procedure

The nonlinear ultrasonic measurements performed on these surrogate specimens consists of the generation of a fundamental frequency sinusoidal wave which travels through the thickness of the material and is received on the other side of the material. Figure 5 displays a schematic of the experimental setup that was used for these nonlinear longitudinal measurements.

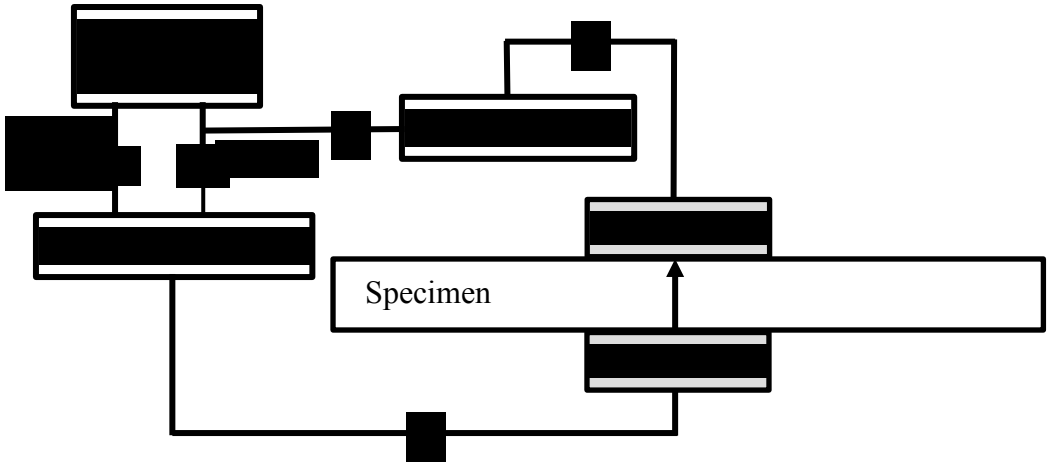

Figure 5. Schematic of Experimental Setup

This experimental setup consists of a 0.5” diameter, Panametrics V106 piezoelectric generating transducer (center frequency of 2.25 MHz) fixed on one side of the specimen and a 0.5” diameter, Panametrics V109 piezoelectric receiving transducer (center frequency of 5 MHz) fixed on the other side of the specimen. Between the transducers and the surface of the specimen, there was a thin layer of light oil coupling. This thin layer of light oil coupling allows for better transmission of acoustic energy directly from the transducer to the material.

The receiving transducer had a center frequency that was twice that of the generating transducer in order to better capture the very small amplitude of the second harmonic wave that was generated in the material. With the amplitude of the first harmonic wave being orders of magnitude larger than that of the second harmonic wave, the receiving transducer was still able to capture the signal well despite the center frequency being closer to that of the second harmonic wave.

Extra care was taken to ensure that the generating and receiving transducers are aligned along their center axis when performing these through thickness measurements. This allows for a direct transmission of the signal. In addition, extra care was also taken to ensure that consistent pressure was applied to each of the transducers when affixing them to the material.

For the measurements that were conducted in this thesis, the fundamental ultrasonic signal was a 6 cycle tone burst at 2.2 MHz generated using a function generator (Agilent 33250A). A tone burst length of 6 cycles was chosen because this is the maximum of cycles that could fit into the thickness of the material (i.e. the longest signal packet that could be used without seeing any effects of reflections). This generated signal was then transmitted to a high-power gated amplifier (RITEC GA-2500A) where the signal was amplified and the input voltage to the transducer could be varied through the use of a dial on the amplifier. From the amplifier, the amplified signal was then transmitted to the generating transducer which in turn transmitted the signal through the thickness of the material. As the wave traveled through the thickness of the material, it interacted with the microstructure of the material (Cu-precipitate pinned dislocations) and generated a second harmonic wave as was described in Section 2.2.2. The receiving transducer on the other side of the material then received the signal.

The received signal was then directly transmitted to an oscilloscope (Tektronix DPO5034B) where the signal was recorded and averaged for 512 averages. The signal was then saved for post-processing that occurred later on. An example of this received signal can be seen in Figure 6. After a single measurement had been saved, the amplitude of the

input voltage was increased (increased amplification) and the next signal was saved. This process continued until the entire input voltage range had been traversed.

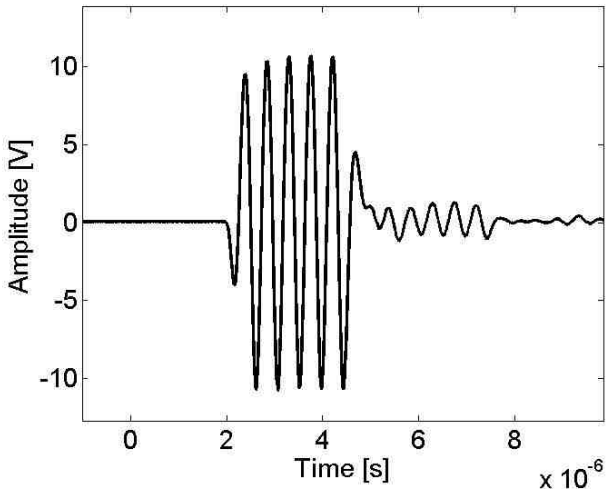

Figure 6. Example Time-domain Signal

5.3 Nonlinear Post-Processing

After all of the signals in the time-domain were recorded for a single sample, post-processing was done in order to extract the amplitudes of the fundamental wave, A_1, and the second harmonic wave, A_2. Typically, a fast Fourier transform (FFT) is performed on these waveforms in order to extract the frequency content. However, the number of cycles that were used in these measurements were too few to be able to use a FFT. When looking at the FFT of the data, it can be seen that the side lobes of the fundamental frequency interfere with the amplitude of the second harmonic which in turn corrupts the data as can be seen in Figure 7.

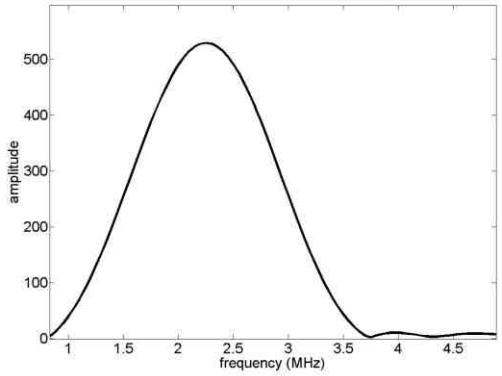

Figure 7. Sample FFT showing interference of side lobes

Therefore, the Prony method, described later in Section 5.3.1 was used to extract the amplitude values for both the fundamental frequency and second harmonic frequency for each of the measured signals. Figure 8 shows a sample of A_1 and A_2 for one of the measurement sets. The measurement number corresponds to a linear increase of the input voltage. As is expected, it is seen that the amplitude of the fundamental frequency and second harmonic increases as the input voltage increases.

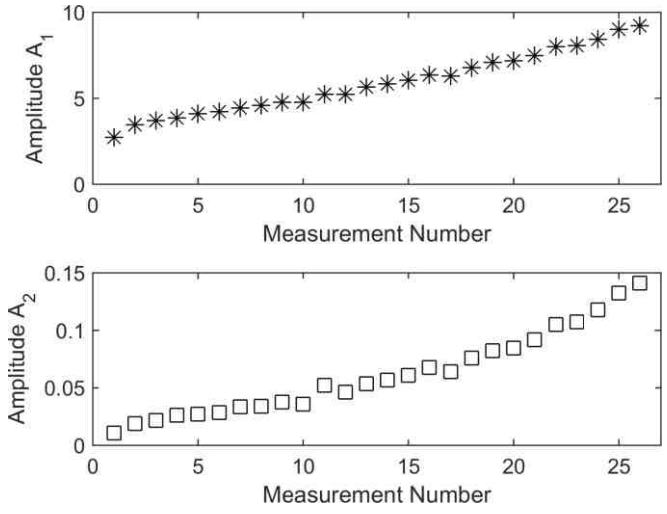

Figure 8. Sample of amplitudes for A_1 and A_2

Once the amplitudes of the harmonics have been extracted, a plot is made of A_2 versus A_1^2 where a linear function was fit to the data. An example plot of this linear fit function and the corresponding A_2 versus A_1^2 data points can be seen in Figure 9. The slope of this linear function is known to be relative β as can be seen earlier in Section 2.1 in Equation (7).

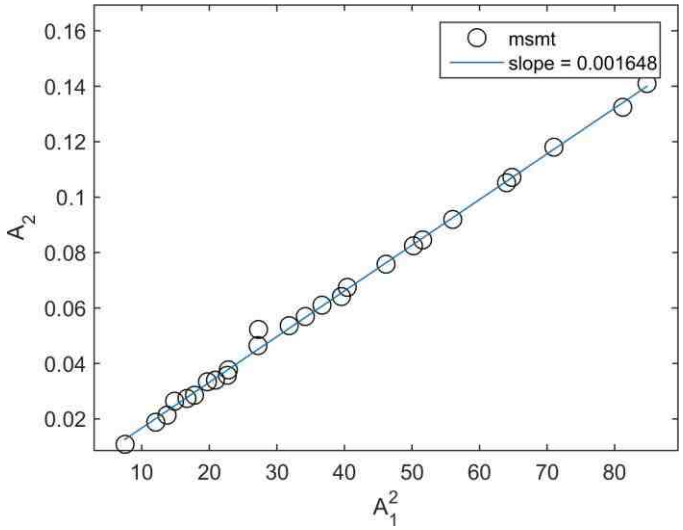

Figure 9. Example of the linear relationship between A_2 and A_1^2

5.3.1 Prony Method

The Prony method is a technique that was developed to fit a linear combination of p exponentials to a set of data points. This technique develops an equation that approximates a discrete data set. These exponentials represent the fundamental and higher harmonics generated as the wave travels through the material. From this technique, information about sinusoidal frequencies, amplitude, phase angle, and damping factor can be determined. In this research, the only information that was of interest was the sinusoidal frequencies and their corresponding amplitudes. The Prony method can be broken down

into three general steps. Step one is developing a model which fits the data and finding the corresponding parameters. Step two finds the roots of a polynomial developed from the parameters. The roots of this polynomial can then be used to determine the frequencies and damping factors. Finally in step 3, all of this information can be used to determine the amplitudes and phase angles. All three steps will be expanded upon and explained in more detail further in the section. It is important to note that the signal investigated with the Prony method must be a finite sample with discrete data points. While the full derivation of the Prony method can be seen here, more information can be found at the following resource [39].

For example, consider the sinusoidal signal that was measured in the nonlinear longitudinal measurements. The Prony prediction model for this sinusoid can be seen in Equation (21) where A_k is the amplitude, α_k is the damping, f_k is the frequency, θ_k is the phase angle, and T is the sampling interval in seconds (1/sampling frequency). Equation (21) can be written in a form that is simpler to solve as can be seen in the second solution of the equation. Equation (22) shows the value of h_k, and Equation (23) shows the value for z_k

$$\hat{x}[n] = \sum_{k=1}^{p} A_k e^{(\alpha_k + k2\pi f_k)(n-1)T + j\theta_k} = \sum_{k=1}^{p} h_k {z_k}^{n-1} \tag{21}$$

$$h_k = A_k e^{j\theta_k} \tag{22}$$

$$z_k = e^{(\alpha_k + k2\pi f_k)T} \tag{23}$$

In this research, there are enough data samples to solve for all of the desired parameters. Therefore, an exact fit to the model can be made. This means $\hat{x}[n] = x[n]$ where $x[n]$ are the exact data points pulled from signal. $x[n]$ has a length of *N* where it will be said that *N=2p*. In this case, $x[n]$ will be the middle 4 cycles of the larger sinusoid (the sinusoid with a lower amplitude is a reflection of the signal), and the sampling frequency, f_s, is 250 MHz. $x[n]$ can be expanded into matrix form as seen in Equation (24).

$$\begin{bmatrix} x[1] \\ x[2] \\ \vdots \\ x[p] \end{bmatrix} = \begin{bmatrix} z_1^0 & z_2^0 & \dots & z_p^0 \\ z_1^1 & z_2^1 & \dots & z_p^1 \\ \vdots & \cdots & \ddots & \vdots \\ z_1^{p-1} & z_2^{p-1} & \cdots & z_p^{p-1} \end{bmatrix} \begin{bmatrix} h_1 \\ h_2 \\ \vdots \\ h_p \end{bmatrix} \tag{24}$$

In order to find the solution to Equation (24), it is desired to solve for z_k separately. In order to do this, consider a p[th] order polynomial $\emptyset(z)$ known as the characteristic equation as seen in Equation (25). This polynomial can be expanded into a power series as seen in Equation (26) where $a[m]$ are complex coefficients and $a[0] = 1$.

$$\emptyset(z) = \prod_{k=1}^{p} (z - z_k) \tag{25}$$

$$\emptyset(z) = \sum_{m=0}^{p} a[m] z^{p-m} \tag{26}$$

Next, shift the indices of Equation (21) from *n* to *n-m* and multiply the entire equation by $a[m]$ as seen in Equation (27).

$$a[m]x[n-m] = a[m]\sum_{k=1}^{p} h_k z_k^{n-m-1} \tag{27}$$

Now take the summation of Equation (27) over *m*=0 to *p* so that the equation is in a similar form to $\emptyset(z)$ as can be seen in Equation (28) which is valid for $p+1 \leq n \leq 2p$.

$$\sum_{m=0}^{p} a[m]x[n-m] = \sum_{k=0}^{p} h_k \sum_{m=0}^{p} a[m] z_k^{n-m-1} \tag{28}$$

Knowing that $z_i^{n-m-1} = z_i^{n-p} z_i^{p-m-1}$ a substitution can be made into Equation (28) resulting in the following equation

$$\sum_{m=0}^{p} a[m]x[n-m] = \sum_{k=0}^{p} h_k z_i^{n-p} \sum_{m=0}^{p} a[m] z_k^{p-m-1} = 0 \tag{29}$$

It can be seen that the third summation in Equation (29) is equal to $\emptyset(z_k)$. Since z_k is a root of $\emptyset(z)$, $\sum_{m=0}^{p} a[m] z_k^{p-m-1}$ is equal to zero and consequently the entire equation (29) is equal to zero. Expanding upon this fact, one can write the left hand side of Equation (29) into matrix notation as seen in Equation (30).

$$\begin{bmatrix} x[p] & x[p-1] & \cdots & x[1] \\ x[p+1] & x[p] & \cdots & x[2] \\ \vdots & \vdots & \ddots & \vdots \\ x[2p-1] & x[2p-2] & \cdots & x[p] \end{bmatrix} \begin{bmatrix} a[1] \\ a[2] \\ \vdots \\ a[p] \end{bmatrix} = -\begin{bmatrix} x[p+1] \\ x[p+2] \\ \vdots \\ x[2p] \end{bmatrix} \tag{30}$$

Using Equation (30) and the least squares method, one can solve for the coefficients, $a[m]$. Now that these coefficients are known, one can solve for the roots of the characteristic

equation. To better understand this characteristic equation, the expanded form can be seen in Equation (31).

$$z^p + a_1 z^{p-1} + \cdots + a_{p-1} z + a_p = (z - z_1)(z - z_2)(\cdots)\left(z - z_p\right) \tag{31}$$

The roots of the characteristic polynomial can then be used to calculate the damping factors and the frequencies as seen in Equations (32) and (33), respectively.

$$\alpha_k = \frac{\ln|z_k|}{T} \ (sec^{-1}) \tag{32}$$

$$f_k = \frac{\tan^{-1}\left(\frac{Im\{z_k\}}{Re\{z_k\}}\right)}{2\pi T} \ (Hz) \tag{33}$$

Since the values of z_k are now known, Equation (24) can be solved for the h_k values using a least squares algorithm. These h_k values can then be used to determine the amplitudes and phase angle values as seen in Equations (34) and (35), respectively.

$$A_k = |h_k| \tag{34}$$

$$\theta_k = \tan^{-1}\left(\frac{Im\{h_k\}}{Re\{h_k\}}\right) \ (radians) \tag{35}$$

The main advantage of the Prony method is that it can be used to decompose short time domain signals into their frequency, amplitude, phase angle, and damping components without the worry of side lobe interference that is seen in FFTs. However, it is important to note that noise has a larger effect on the Prony method than on the FFT. In these

measurements, the signal to noise ratio was very high and averaging of the measurements improves the signal to noise ratio even more.

5.4 Linear Ultrasonic Measurements

5.4.1 Attenuation

The attenuation measurements were made by using an immersion technique as is depicted in Figure 10. As can be seen in the figure, these measurements make use of the pulse-echo method [40] where a pulse is generated and sent into the water. The pulse then travels through the water and through the thickness of the specimen where is reflected off the back wall and travels back through the thickness of the material. When this wave reaches the front wall, part of the wave is transmitted to the receiver while part of the wave is reflected back towards the back wall. This wave propagation provides the two reflections that were measured by the oscilloscope and used for the attenuation calculations.

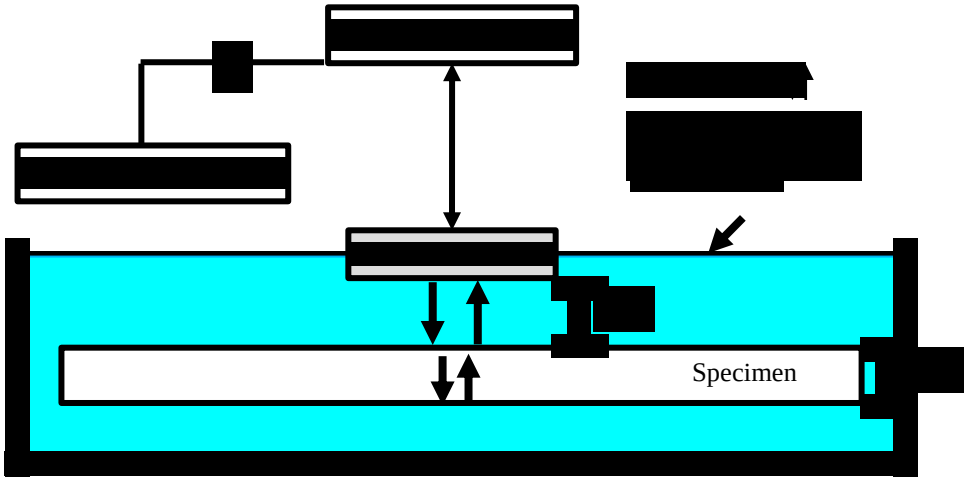

Figure 10. Schematic for Attenuation Measurements

A sample signal for the attenuation measurements can be seen in Figure 11. In the figure, the reflections from the specimen can be seen. Next, a Hann window was placed around each of the reflections and a FFT was taken in Matlab to determine the frequency spectrum of each reflection.

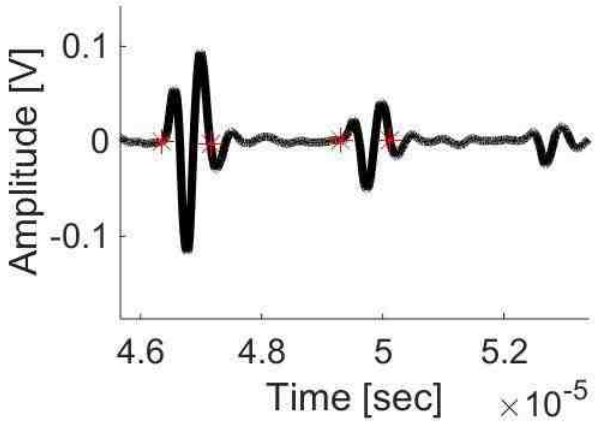

Figure 11. Attenuation Time Domain Signal

After the frequency spectrum was obtained, the attenuation at a particular frequency can be calculated according to Equation (36) where h_1 and h_2 are the distances depicted in

Figure 10, k_1 is the wavenumber in the water for a particular frequency, k_2 is the wavenumber in the material for a particular frequency, D_p is diffraction correction calculated using Equation (37), a is the diameter of the transducer, V_1 is the amplitude of the first reflection at a particular frequency, and V_2 is the amplitude of the second reflection at a particular frequency.

$$\alpha(f) = \frac{1}{2h_2} \ln \left| e^{2ik_2h_2} \frac{{R_{21}}^2 D_p\left(\frac{k_1a^2}{2(h_1+2h_2)}\right)}{D_p\left(\frac{k_1a^2}{2(h_1+h_2)}\right)} \frac{V_1}{V_2} \right| \tag{36}$$

$$D_p(s) = \left|1 - e^{-is}\left(J_0(s) + iJ_1(s)\right)\right| \tag{37}$$

5.4.2 Longitudinal Wave Velocity

The longitudinal wave velocity for the surrogate specimens used was calculated using the data already taken for making the attenuation calculations. The time of flight, t_f, between the maximum of the first and second reflections was measured and then used to calculate the longitudinal velocity of the specimen as seen in Equation (38).

$$c_l = \frac{2 * thickness}{t_f} \tag{38}$$

CHAPTER 6. RESULTS AND DISCUSSION

6.1 Overview

This chapter presents the experimental and theoretical results for these surrogate specimens. Using the procedure presented in CHAPTER 5, nonlinear ultrasonic measurements using the SHG technique were made on both sets of surrogate specimens (Fe-1.0% Cu and Fe-0.1% Cu). For each of the specimens, five measurement sets were made in order to determine the consistency and repeatability of the measurements. Additionally, a theoretical prediction was made as a comparison to the experimental results.

6.2 Nonlinear Ultrasonic Results

The experimental results for relative β for the Fe-1.0% Cu specimens can be seen in Figure 12. Since the thickness of each specimen (propagation distance) is equal and the same frequency was used for each measurement set, the results for β are the ratio of $\frac{A_2}{A_1^2}$ where the amplitude of A_2 and A_1 is in volts.

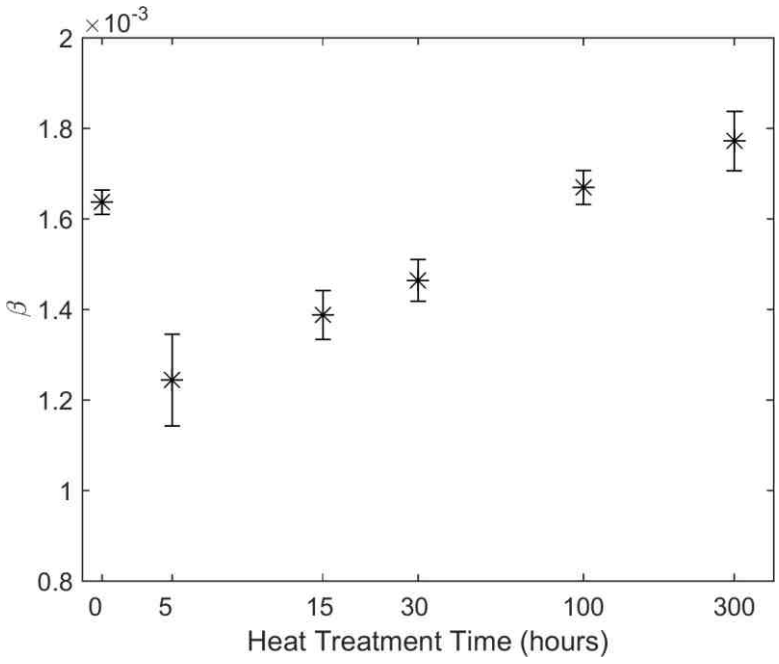

Figure 12. Relative β for Fe-1.0% Cu Specimens

Each measurement point represents an average of 5 measurement sets, and the error bars are the standard error for each of the heat treatment times. As can be seen in Figure 12, there is a significant change in β as the heat treatment time increases. There is an initial drop in β from the baseline state to the 5-hour heat treatment time, that is assumed to be due to the initial nucleation of Cu-precipitates; a similar behavior was seen in [18]. Cantrell and Yost [41] observed an increase of β for a short period in the very beginning followed by a decrease. In this measurement, this initial increase might have been missed to the small number of data points for short heat treatment periods. After the initial drop for the 5-hour specimen, the measured β increases with increasing heat treatment time. This increase for the 5-hour to the 30-hour specimens is due to an increase in the radius of the Cu precipitates with increasing heat treatment time as evidenced by the SANS results of Figure 2. After the 30-hour specimen, there is a coarsening effect and a loss of coherency as evidenced by Figure 3 with a decrease in hardness. However, there is still an increase in

β which may be due to one of two reasons. One reason is that some of the Cu-precipitates will remain coherent with the Fe-matrix which would result in a continued increase in β. The second reason is as the Cu-precipitates transform from a BCC structure to a 9R structure some of the dislocations will become unpinned. While it might be expected that this would lead to a decrease in β, it actually might cause a compounding effect where the total nonlinearity parameter is a combination of β due to the increase in precipitate radii as well as β due to the dislocations in the material.

It is also seen in the figure that the measurements for the Fe-1.0% Cu specimens produced sufficiently small error bars. Experimental conditions that contribute to the size of these error bars include inconsistencies in coupling conditions between measurement sets and inconsistencies in clamping force between measurement sets. Knowing that these inconsistencies lead to variations in determination of β, it is very important to take as much care as possible when preparing the experimental setup. To provide more consistency for the coupling conditions, the specimen and transducers should be wiped down using a smooth cloth in between each measurement set, and the same amount of light-oil couplant should be applied to the transducers each time.

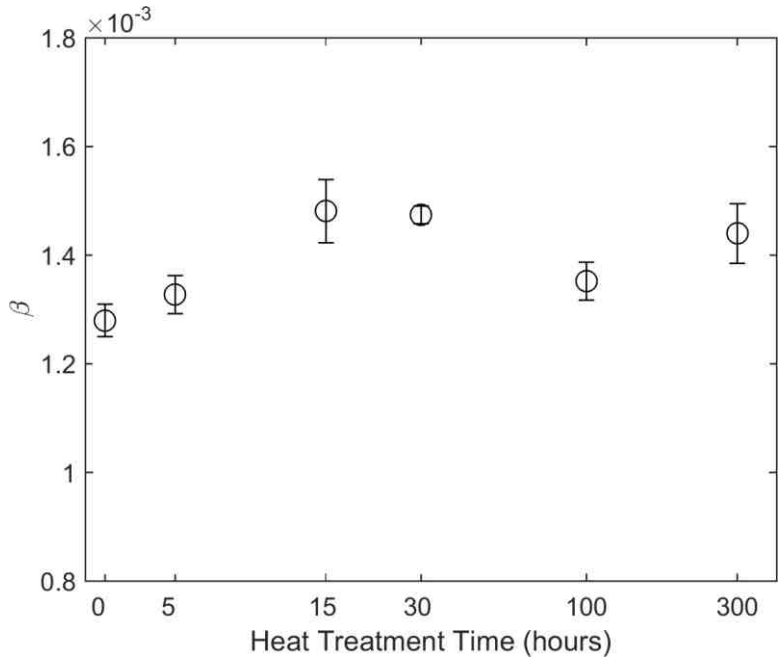

Figure 13. Relative β for Fe-0.1% Cu Specimens

Figure 13 shows the experimental results for the Fe-0.1% Cu specimens. As can be seen in the figure, these results are not conclusive. It can be seen that on average there is a slight increasing trend in β. However, this increase in β is still within the range of the error bars. This is because the Cu content is too small for the precipitation to occur in the same time scale as in the 1% specimens. However, the small up-and-down behavior may be corresponding to the same behavior in Cantrell and Yost [41]. In other words, the same phenomenon occurs over extended time scale and with much smaller magnitude. This hypothesis is to be validated in a further research.

6.3 Theoretical Model

The theoretical model for the nonlinearity parameter developed for this thesis is based on the model for precipitate pinned dislocations developed by Cantrell and Yost [18] as seen in Section 2.2.2. While the model provides a great model for the effect of precipitate

pinned dislocations on the nonlinearity parameter, it does not account for instances when the elastic properties of the matrix and precipitate are not equivalent. In order to account for this difference in elastic properties, Hurley et al developed a new expression for the radial stress around the precipitate [13].

This expression for the average stress on a dislocation segment can be seen in Equation (39) where B is the bulk modulus of the precipitate and G is the shear modulus of the material.

$$|\sigma| = 2|\sigma_{rr}| = \frac{64Gr_1^3\delta}{(L)^3}\left[\frac{3B}{3B+4G}\right] \tag{39}$$

Plugging this equatoin for the average stress into the model developed by Cantrell and Yost (Equation (20)), one gets the expression for the change in the nonlinearity parameter due to these precipitate pinned dislocations as given in Equation (40). This model assumes that the average precipitate radius is the critical radius, and that all of the growing precipitates are at the critical size.

$$\Delta\beta = 495\frac{\Omega\Lambda R^3 {C_{11}}^2|\delta|{r_{avg}}^4}{G^2b^2{f_n}^{1/3}}\left[\frac{3B}{3B+4G}\right] \tag{40}$$

All of the variables in Equation (40) except for the average radius remain constant for all of the specimens. Therefore, their values were found in the literature, except for the volume fraction which was calculated from the weight percentage of Cu in the material. The average radius was determined from the SANS measurements that were made on the specimens and seen in Table 1.

The values for the constants found in Equation (40) are summarized in Table 2. These values were determined by consulting the literature and confirming their value with multiple papers. The lattice misfit parameter was calculated by finding the percent change in the lattice parameter from that of pure α-iron to that of the Fe-Cu matrix.

Table 2. Constants for Theoretical Model

Burgers Vector, b	Dislocation Density, Λ	2nd Elastic Constant, C_{11}	Shear Modulus, G	Schmid Factor, R	γ strain to ε strain, Ω	Lattice Misfit, δ	Bulk modulus, B
2.48 Å [42-44]	$6x10^{13}$ m^{-2} [44-46]	286 GPa [45, 47]	83 GPa [42-44]	0.3 [13, 18]	0.3 [13, 18]	1.4% [48, 49]	140 GPa [13]

The volume fraction of Cu-precipitates was calculated from the percent weight of Cu in the material which is known to be 1.0%. Knowing this, the weight of Cu in the material can be calculated by multiplying the total weight of the specimen (333 g) by 1.0%, giving 3.33 g of Cu in the material. The volume of Cu, v_{Cu}, in the material can be found by dividing this mass of Cu by the density of Cu, 8940 kg/m^3 [50] ($3.72x10^{-7}m^3$). The volume fraction of Cu, f_n, can then be calculated by using Equation (41) where v_{total} is the total volume of the material. The total volume of the material can be found by adding the volumes of Cu and Fe. The volume of Fe is found in the same manner as the volume for Cu was found (density of Fe is 7870 kg/m^3 [50]).

$$f_n = \frac{v_{Cu}}{v_{total}} = 0.89\% \tag{41}$$

Now that the values for the constants, volume fraction, and precipitate radius are known, they can be plugged into the model to find $\Delta\beta$ for each of the heat treatment times.

While the change in the nonlinearity parameter shows the trend of the nonlinearity in the material as heat treatment time increases, it does not allow for a comparison between the theoretical model and the experimental results. In order to make this comparison, the total nonlinearity parameter in the material needs to be calculated and then normalized by the undamaged state of the material. The total nonlinearity parameter is equal to $\Delta\beta$ plus the nonlinearity parameter of the undamaged Fe polycrystal, β_L. β_L is found in the literature to be 8.76 [51] and can also be calculated using Equation (3).

Figure 14 displays the results of the theoretical model for the Fe-1.0% Cu specimens. The radii size for the Fe-0.1% Cu specimens was not measured so the theoretical model was not applied for these specimens. It should be noted that the theoretical model was only calculated for the 5-hour through 30-hour specimens. This is because the model is no longer valid after the start of coarsening. As can be seen in the figure, there is an increasing trend in β as the heat treatment time increases.

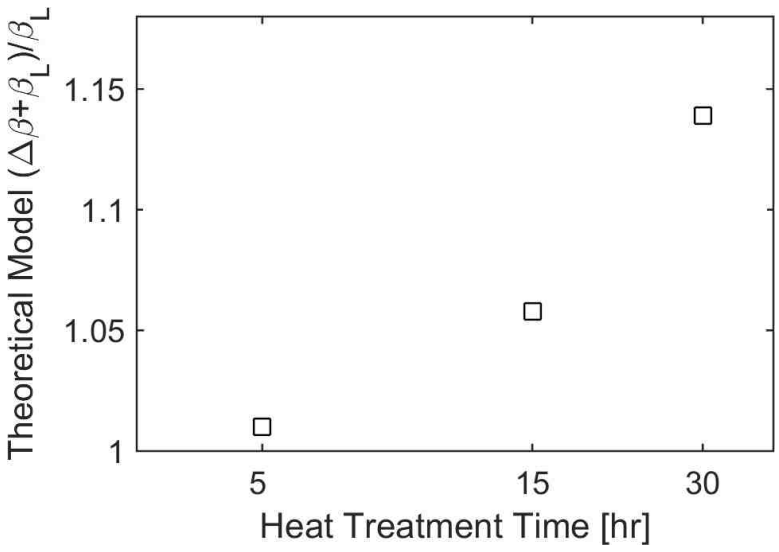

Figure 14. Theoretical Model for β for Fe-1.0% Cu specimens

6.4 Comparison between Experimental Results and Theoretical Results

Now that the experimental results and theoretical model for the Fe-1.0% Cu specimens have been calculated a comparison can be made between the two. In order to make a comparison with the normalized theoretical β, the experimental results are normalized by the value of the 5-hour specimen. The 5-hour specimen is used to normalize the data because it is the first heat treatment time after the nucleation of the Cu-precipitates. Figure 15 shows the graphical comparison between these two sets of data. As can be seen in the figure, both the experimental data and theoretical model have very similar increasing trends in β as the thermal aging of the material increases. The increase in β for the theoretical model from the 5-hour specimen to the 30-hour specimen is 14% and the increase in β for the experimental data from the 5-hour specimen to the 30-hour specimen is 18%. The overall increase in the experimental data from the 5-hour specimen to the 300-hour specimen is 42%. These significant increases in β demonstrate the sensitivity of NLU to these Cu-precipitates.

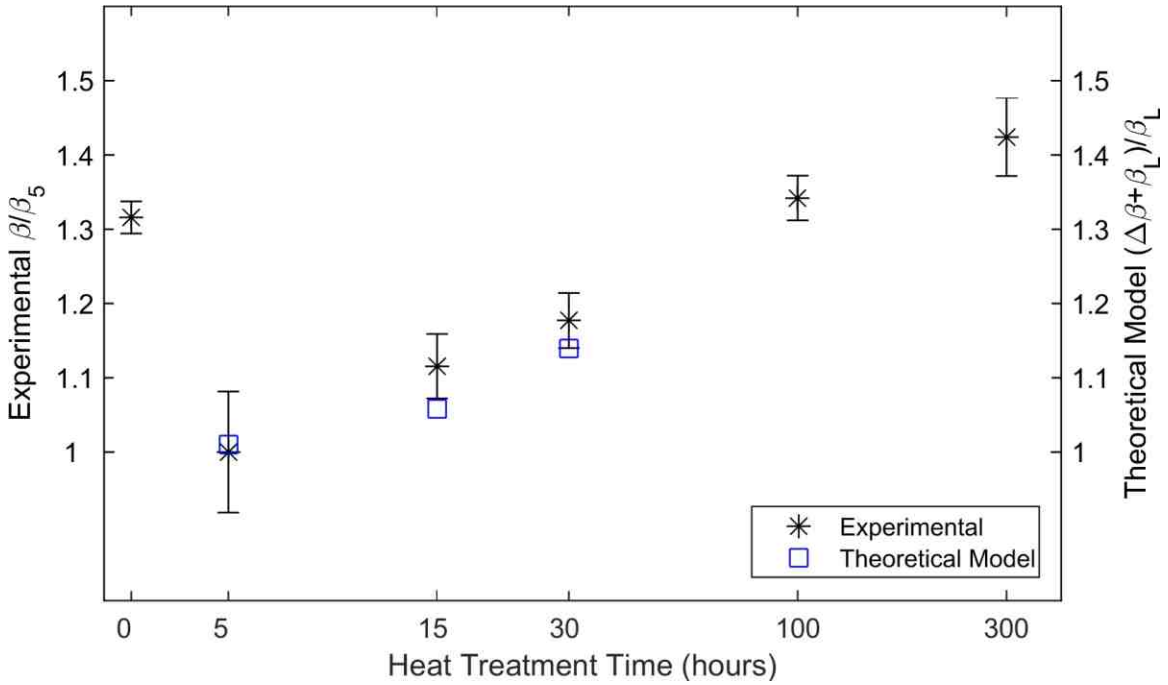

Figure 15. Comparison between experimental β and theoretical β for Fe-1.0% Cu specimens

6.5 Linear Ultrasonic Results

While the focus of this research is on SHG using NLU, linear ultrasonic measurements, attenuation and velocity, were made as a comparison. As discussed in Chapter 1, linear ultrasound is not very sensitive to changes in the microstructure where the micro-damage is much smaller than the wavelength of the introduced wave. This lack of sensitivity will be seen in the linear measurements that follow because in this research, the "micro-damage" comes in the form of Cu-precipitates whose radii are on the order of nanometers whereas the wavelength of the fundamental frequency approximately 3 mm.

6.5.1 Attenuation

The immersion technique, described in Section 5.4.1, used to measure the attenuation avoids the complications and inconsistencies that arise in contact measurements. It allows for more consistent and better coupling conditions between the transducer and the specimen. However, this method would be impractical and very difficult to implement in the field.

The results for attenuation of the Fe-1.0% Cu specimens as a function of frequency can be seen in Figure 16. Figure 17 shows the attenuation of the specimens at 2.25 MHz (center frequency of generating transducer) as a function of heat treatment time. As can be seen in the figure, there is not as large of a change in the attenuation of the specimens throughout the thermal aging as there was change in β. There is a decrease in attenuation as heat treatment time increases until the 100-hour specimen and then there is an increase in the attenuation. This trend in attenuation was also seen by Hurley et al who made linear and nonlinear measurements on ASTM A710 specimens which contained Cu-rich precipitates [13]. However, Hurley et al did not know the cause of this decrease and then increase in attenuation. Additionally, this decrease in attenuation and then increase in attenuation was seen by Matlack for a set of irradiated specimens [52] where the attenuation decreased from the unirradiated state to medium fluence and the increased from medium fluence to high fluence.

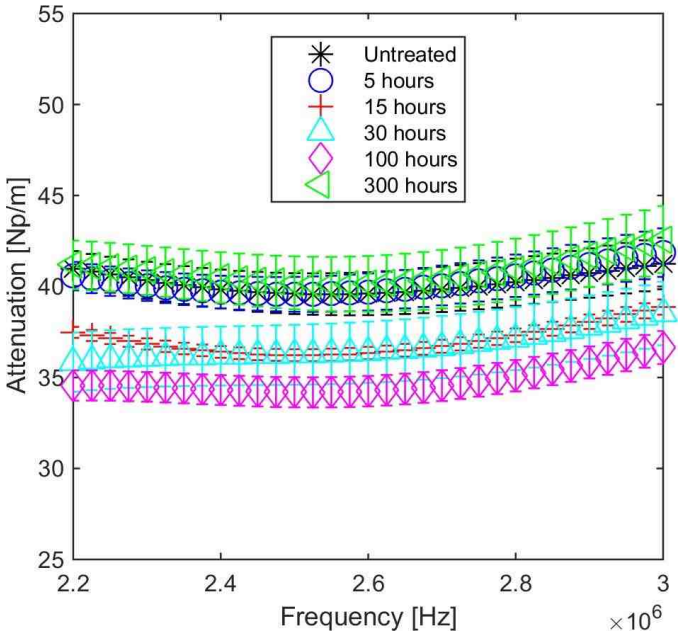

Figure 16. Attenuation of Fe-1.0% Cu Specimens

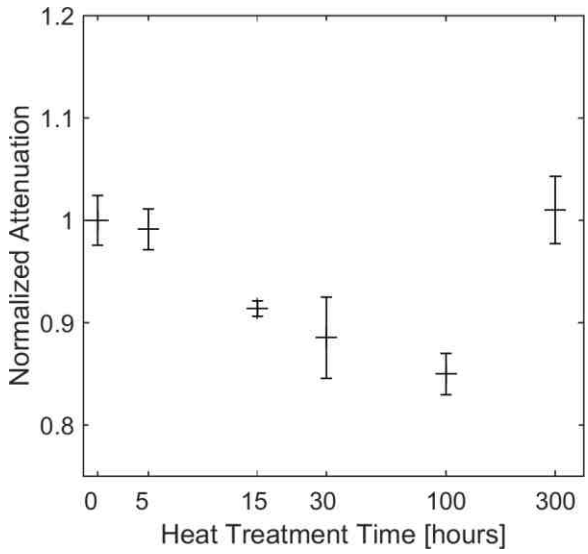

Figure 17. Attenuation of Fe-1.0% Cu specimens at 2.25 MHz

6.5.2 Velocity

Figure 18 shows the results for the longitudinal velocity in the Fe-1.0% Cu surrogate specimens. As can be seen in the figure, the Cu-precipitates seem to have no effect on the velocity in the material where the change in velocity from the untreated specimen to the 300-hour specimen is only 1%.

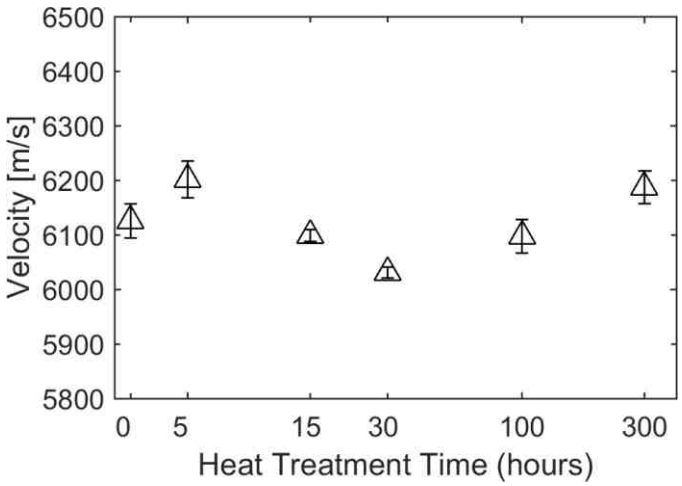

Figure 18. Velocity of Fe-1.0% Cu Specimens

6.6 Comparison Linear and Nonlinear Measurements

From these measurements, a comparison can be made between the measurements of β and longitudinal velocity for the Fe-1.0% Cu specimens. Attenuation will not be compared because of its unexpected behaviour. Figure 19 shows a comparison between the normalized β values for the Fe-1.0% Cu specimens and the normalized longitudinal velocity values for the Fe-1.0% Cu specimens. As can be seen in the figure, the increase in β is approximately 42% while the change in the velocity is only about 1%. This comparison demonstrates the difference in the sensitivity to the Cu-precipitates of the two different

methods. It shows that NLU is much more sensitive to these nanoscale changes in the Fe-1.0% Cu material than linear ultrasound is.

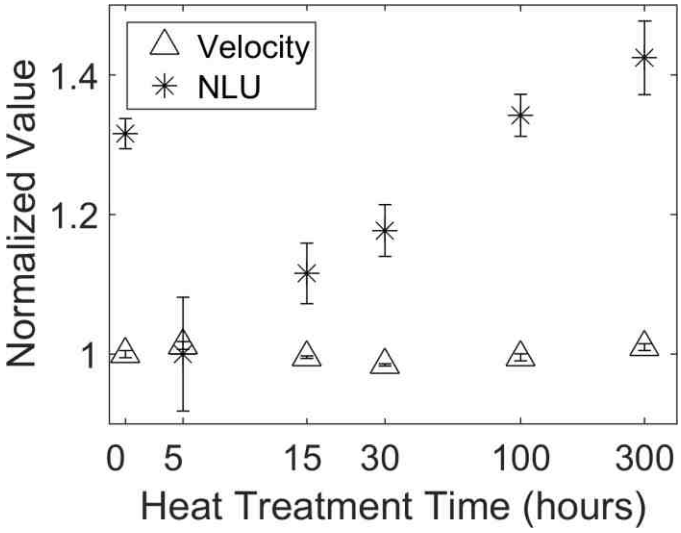

Figure 19. Comparison between normalized β and normalized longitudinal velocity for Fe-1.0% Cu specimens

CHAPTER 7. CONCLUSION AND FUTURE WORK

7.1 Overview

This chapter provides a conclusion to the work that was completed for this thesis and an outlook to future work that could be completed to further work in this area.

7.2 Conclusion

The measurements made on these Fe-Cu specimens show the sensitivity of SHG to the formation of Cu-precipitates if the Cu content is high enough. The results for the Fe-1.0% Cu specimens show a definitive increasing trend in β as thermal aging increases. Initially, it is seen that β decreases from the baseline state to the 5-hour specimen. This decrease in β is due to the nucleation of Cu-precipitates. After this initial period, it is seen that β increases with heat treatment. For the 5-hour through 30-hour specimens, this increase is attributed to the growth of Cu-precipitates. However, for the 100-hour and 300-hour specimens, the exact reason for the increase in β is unknown. The increase is either due to not all of the precipitates transforming to an incoherent state or due to both the precipitate growth as well as free dislocation contributing to β. From the 5-hour specimen to the 300 hour specimen, it is seen that β increases significantly by approximately 42%.

These experimental results are complimented by the results of a theoretical model. The theoretical model relates the material properties, volume fraction of Cu-precipitates, and radii of Cu-precipitates to the nonlinearity parameter. As was seen in the experimental results, the theoretical model shows that β increases as the radii of the Cu-precipitates increase.

In contrast to the Fe-1.0% Cu specimens, the results for the Fe-0.1% Cu specimens were inconclusive. It was seen that β had a slight increasing trend as heat treatment time increased but was insignificant and very inclusive. These results show that the Cu content in the Fe-0.1% Cu specimens was not large enough to be detected by SHG. Additionally, the results of the linear measurements, velocity and attenuation, show very little variation in the measurements as the heat treatment time increases.

7.3 Future Work

This research demonstrates the sensitivity of NLU to Cu-precipitates if the Cu content is large enough. However, more work needs to be done in order to detect Cu-precipitates in materials where the volume fraction of Cu is lower. This lower volume fraction of Cu would be a better representation of RPV steel where the largest amount of Cu is found to be around 0.5% [25]. Additionally, newer nuclear reactors are being made with even less Cu (around 0.01%). Higher sensitivity to Cu-precipitates would allow for a better comparison to these newer reactors.

This research only provides results from the SHG technique of using longitudinal waves that propagate through the thickness of the material. It would be desirable to be able to use Rayleigh waves to measure the nonlinearity of the material. One benefit of Rayleigh wave measurements is being able to make measurements only on one side of the material. This provides a benefit when one side of the material cannot be accessed. Another benefit of Rayleigh wave measurements is the reduction in the influence of system nonlinearity. With these benefits, it seems like Rayleigh wave measurements would be the obvious choice. However, it was found that with the current systems Rayleigh wave measurements

cannot be made on this material. When attempting to make the Rayleigh wave measurements, it was found that the attenuation in the material was so large that the received signal was lost in the noise. Note that the attenuation of Rayleigh waves is about twice higher than that of longitudinal waves at the same frequency. Additional study of the material and setup would need to be done to be able to perform these Rayleigh wave measurements.

Additional microscopy and material study needs to be done to better link the change in β to the microstructure of the material. The exact reason for the continued increase in β for the 100-hour and 300-hour specimens is unclear. Therefore, more work could be done to link β to the changes in the microstructure.

It would also be of interest to heat treat the specimens for even longer period of time to provide even larger Cu-precipitates where the matrix transforms to the FCC structure. NLU measurements on these specimens would provide more insight to the connection from the material to β.

REFERENCES

[1] K.H. Matlack, H.A. Bradley, S. Thiele, J.-Y. Kim, J.J. Wall, H.J. Jung, J. Qu, L.J. Jacobs, Nonlinear ultrasonic characterization of precipitation in 17-4PH stainless steel, NDT & E International 71 (2015) 8-15.

[2] K.H. Matlack, J.Y. Kim, J.J. Wall, J. Qu, L.J. Jacobs, M.A. Sokolov, Sensitivity of ultrasonic nonlinearity to irradiated, annealed, and re-irradiated microstructure changes in RPV steels, Journal of Nuclear Materials 448(1–3) (2014) 26-32.

[3] K.H. Matlack, J.-Y. Kim, J. Wall, J. Qu, L. Jacobs, Using nonlinear ultrasound to measure microstructural changes due to radiation damage in steel, Proceedings of Meetings on Acoustics 19(1) (2013) 045023.

[4] K.H. Matlack, J.J. Wall, J.-Y. Kim, J. Qu, L.J. Jacobs, H.-W. Viehrig, Evaluation of radiation damage using nonlinear ultrasound, Journal of Applied Physics 111(5) (2012) 054911.

[5] A.V. Barashev, S.I. Golubov, D.J. Bacon, P.E.J. Flewitt, T.A. Lewis, Copper precipitation in Fe–Cu alloys under electron and neutron irradiation, Acta Materialia 52(4) (2004) 877-886.

[6] P. Erhart, J. Marian, B. Sadigh, Thermodynamic and mechanical properties of copper precipitates in $\ensuremath{\alpha}$-iron from atomistic simulations, Physical Review B 88(2) (2013) 024116.

[7] S.I. Golubov, Y.N. Osetsky, A. Serra, A.V. Barashev, The evolution of copper precipitates in binary Fe・Cu alloys during ageing and irradiation, Journal of Nuclear Materials 226(1) (1995) 252-255.

[8] Y. Nagai, Z. Tang, M. Hassegawa, T. Kanai, M. Saneyasu, Irradiation-induced Cu aggregations in Fe: An origin of embrittlement of reactor pressure vessel steels, Physical Review B 63(13) (2001) 134110.

[9] K.H. Matlack, J.-Y. Kim, L.J. Jacobs, J. Qu, Review of Second Harmonic Generation Measurement Techniques for Material State Determination in Metals, Journal of Nondestructive Evaluation 34(1) (2014) 273.

[10] A. Hikata, B.B. Chick, C. Elbaum, Dislocation Contribution to the Second Harmonic Generation of Ultrasonic Waves, Journal of Applied Physics 36(1) (1965) 229-236.

[11] J.H. Cantrell, W.T. Yost, Nonlinear ultrasonic characterization of fatigue microstructures, International Journal of Fatigue 23, Supplement 1 (2001) 487-490.

[12] A. Metya, M. Ghosh, N. Parida, S. Palit Sagar, Higher harmonic analysis of ultrasonic signal for ageing behaviour study of C-250 grade maraging steel, NDT & E International 41(6) (2008) 484-489.

[13] D. Hurley, D. Balzar, P. Purtscher, Nonlinear ultrasonic assessment of precipitation hardening in ASTM A710 steel, Journal of Materials Research 15(09) (2000) 2036-2042.

[14] A. Viswanath, B.P.C. Rao, S. Mahadevan, T. Jayakumar, B. Raj, Microstructural characterization of M250 grade maraging steel using nonlinear ultrasonic technique, Journal of Materials Science 45(24) (2010) 6719-6726.

[15] H. Jeong, S.-H. Nahm, K.-Y. Jhang, Y.-H. Nam, A nondestructive method for estimation of the fracture toughness of CrMoV rotor steels based on ultrasonic nonlinearity, Ultrasonics 41(7) (2003) 543-549.

[16] A.N. Norris, Nonlinear Acoustics, Acoustical Society of America, Melville, NY, 1998.

[17] M.A. Breazeale, D.O. Thompson, FINITE-AMPLITUDE ULTRASONIC WAVES IN ALUMINUM, Applied Physics Letters 3(5) (1963) 77-78.

[18] J.H. Cantrell, W.T. Yost, Determination of precipitate nucleation and growth rates from ultrasonic harmonic generation, Applied Physics Letters 77(13) (2000) 1952-1954.

[19] M. Blaszkiewicz, The development of nondestructive evaluation (NDE) for monitoring the embrittlement in nuclear reactor pressure vessels, Materials Science Forum, Trans Tech Publ, 1996, pp. 9-16.

[20] G.R. Odette, G.E. Lucas, Embrittlement of nuclear reactor pressure vessels, JOM 53(7) (2001) 18-22.

[21] W.A. Pavinich, T.J. Griesbach, W.L. Server, An overview of radiation embrittlement modeling for reactor vessel steels, Radiation Embrittlement of Nuclear Reactor Pressure Vessel Steels: An International Review (Fourth Volume), ASTM International1993.

[22] M. Akamatsu, J.C. Van Duysen, P. Pareige, P. Auger, Experimental evidence of several contributions to the radiation damage in ferritic alloys, Journal of Nuclear Materials 225 (1995) 192-195.

[23] R.G. Carter, N. Soneda, K. Dohi, J.M. Hyde, C.A. English, W.L. Server, Microstructural characterization of irradiation-induced Cu-enriched clusters in reactor pressure vessel steels, Journal of Nuclear Materials 298(3) (2001) 211-224.

[24] B.A. Gurovich, E.A. Kuleshova, Y.A. Nikolaev, Y.I. Shtrombakh, Assessment of relative contributions from different mechanisms to radiation embrittlement of reactor pressure vessel steels, Journal of Nuclear Materials 246(2) (1997) 91-120.

[25] W.J. Phythian, C.A. English, Microstructural evolution in reactor pressure vessel steels, Journal of Nuclear Materials 205 (1993) 162-177.

[26] G. Odette, On the dominant mechanism of irradiation embrittlement of reactor pressure vessel steels, Scripta metallurgica 17(10) (1983) 1183-1188.

[27] G.R. Odette, G.E. Lucas, Irradiation embrittlement of reactor pressure vessel steels: mechanisms, models, and data correlations, Radiation Embrittlement of Nuclear Reactor Pressure Vessel Steels: An International Review (Second Volume), ASTM International1986.

[28] J.R. Hawthorne, Irradiation embrittlement, Embrittlement of engineering alloys 25 (2013) 461-524.

[29] A. Barbu, T.N. Le, N. Lorenzelli, F. Maury, C.H. Novion, Formation of copper-rich precipittes by electron irradiation or by thermal treatment in model iron-based alloys, Annales de Chimie Science des Materiaux (Paris) 16(4-6) (1991) 325-331.

[30] J.J. Blackstock, G.J. Ackland, Phase transitions of copper precipitates in Fe–Cu alloys, Philosophical Magazine A 81(9) (2001) 2127-2148.

[31] M. Charleux, F. Livet, F. Bley, F. Louchet, Y. Bréchet, Thermal ageing of an Fe[sbnd]Cu alloy: Microstructural evolution and precipitation hardening, Philosophical Magazine A 73(4) (1996) 883-897.

[32] S. Hu, Y. Li, K. Watanabe, Calculation of internal stresses around Cu precipitates in the bcc Fe matrix by atomic simulation, Modelling and simulation in materials science and engineering 7(4) (1999) 641.

[33] P.J. Othen, M.L. Jenkins, G.D.W. Smith, High-resolution electron microscopy studies of the structure of Cu precipitates in α-Fe, Philosophical Magazine A 70(1) (1994) 1-24.

[34] L.P. Vandenbossche, M.J. Konstantinović, A. Almazouzi, L.R. Dupré, Magnetic evaluation of the hardening and softening of thermally aged iron–copper alloys, Journal of Physics D: Applied Physics 40(14) (2007) 4114.

[35] Y.-S. Han, D.-G. Park, S. Kobayashi, Small Angle Neutron Scattering Study of Nano Sized Precipitates in Ferrous Alloys, Journal of nanoscience and nanotechnology 15(11) (2015) 8608-8612.

[36] L. Yi, L. Yuanfei, D. Shanquan, X. Ben, L. Qiulin, S. Guogang, L. Wei, Changes in the magnetic and mechanical properties of thermally aged Fe–Cu alloys due to nano-sized precipitates, Journal of Physics D: Applied Physics 49(3) (2016) 035006.

[37] A. Youle, B. Ralph, A Study of the Precipitation of Copper from α-Iron in the Pre-Peak to Peak Hardness Range of Ageing, Metal Science Journal 6(1) (1972) 149-152.

[38] D.G. Park, K.S. Ryu, S. Kobayashi, S. Takahashi, Y.M. Cheong, Change in magnetic properties of a cold rolled and thermally aged Fe–Cu alloy, Journal of Applied Physics 107(9) (2010) 09A330.

[39] S.L. Marple, Digital Spectral Analysis with Applications, Prentice-Hall, INC., New Jersey, 1987.

[40] T. Kang, H.-H. Kim, S.-J. Song, H.-J. Kim, Characterization of fatigue damage of Al6061-T6 with ultrasound, NDT & E International 52 (2012) 51-56.

[41] J.H. Cantrell, W.T. Yost, Effect of precipitate coherency strains on acoustic harmonic generation, Journal of Applied Physics 81(7) (1997) 2957-2962.

[42] K.C. Russell, L. Brown, A dispersion strengthening model based on differing elastic moduli applied to the iron-copper system, Acta Metallurgica 20(7) (1972) 969-974.

[43] S. Schmauder, P. Binkele, Atomistic computer simulation of the formation of Cu-precipitates in steels, Computational materials science 24(1) (2002) 42-53.

[44] J. YANG, M. ENOMOTO, Numerical simulation of copper precipitation during aging in deformed Fe-Cu alloys, ISIJ international 45(9) (2005) 1335-1344.

[45] C. Zhang, M. Enomoto, T. Yamashita, N. Sano, Cu precipitation in a prestrained Fe-1.5 wt pct Cu alloy during isothermal aging, Metallurgical and Materials Transactions A 35(4) (2004) 1263-1272.

[46] J. Zhao, Q. Wang, H. Li, J. He, Modeling of the Precipitation Kinetics During Aging a Predeformed Fe-Cu Alloy, Metallurgical and Materials Transactions A 42(10) (2011) 3200-3207.

[47] G. Ackland, D. Bacon, A. Calder, T. Harry, Computer simulation of point defect properties in dilute Fe—Cu alloy using a many-body interatomic potential, Philosophical Magazine A 75(3) (1997) 713-732.

[48] F. Maury, N. Lorenzelli, M. Mathon, C. De Novion, P. Lagarde, Copper precipitation in FeCu, FeCuMn, and FeCuNi dilute alloys followed by X-ray absorption spectroscopy, Journal of Physics: Condensed Matter 6(2) (1994) 569.

[49] F. Soisson, A. Barbu, G. Martin, Monte Carlo simulations of copper precipitation in dilute iron-copper alloys during thermal ageing and under electron irradiation, Acta Materialia 44(9) (1996) 3789-3800.

[50] W.D. Callister, Materials Science and Engineering: An Introduction, Seventh ed., John Wiley & Sons, Inc.2007.

[51] C.M. Kube, J.A. Turner, Acoustic nonlinearity parameters for transversely isotropic polycrystalline materials, The Journal of the Acoustical Society of America 137(6) (2015) 3272-3280.

[52] K.H. Matlack, Nonlinear Ultrasound for Radiation Damage Detection, GW Woodruff School of Mechanical Engineering, Georgia Institute of Technology, Atlanta, GA, 2014, p. 168.